



Automated prescreening of pigmented skin lesions using standard cameras

Pablo G. Cavalcanti, Jacob Scharcanski*

Instituto de Informática, Universidade Federal do Rio Grande do Sul, Avenida Bento Gonçalves 9500, Porto Alegre, RS 91501-970, Brazil

ARTICLE INFO

Article history:

Received 8 September 2010

Accepted 22 February 2011

Keywords:

Computer-aided diagnosis

Pigmented skin lesion

Melanoma

Classification

Standard cameras

ABSTRACT

This paper describes a new method for classifying pigmented skin lesions as benign or malignant. The skin lesion images are acquired with standard cameras, and our method can be used in telemedicine by non-specialists. Each acquired image undergoes a sequence of processing steps, namely: (1) preprocessing, where shading effects are attenuated; (2) segmentation, where a 3-channel image representation is generated and later used to distinguish between lesion and healthy skin areas; (3) feature extraction, where a quantitative representation for the lesion area is generated; and (4) lesion classification, producing an estimate if the lesion is benign or malignant (melanoma). Our method was tested on two publicly available datasets of pigmented skin lesion images. The preliminary experimental results are promising, and suggest that our method can achieve a classification accuracy of 96.71%, which is significantly better than the accuracy of comparable methods available in the literature.

© 2011 Elsevier Ltd. All rights reserved.

1. Introduction

Pigmented skin lesions include both, benign and malignant forms. Melanoma is a kind of malignant pigmented skin lesion, and currently is among the most dangerous existing cancers, resulting in about 10,000 deaths from the 40,000 to 50,000 diagnosed cases per year, just in United States of America [1]. According to World Health Organization [2], about 132,000 melanoma cases occur globally each year. Benign pigmented skin lesions are called moles, or nevi. However, differentiating benign and malignant lesions can be challenging. For example, there are nevi known as Clark Nevi (also referred as Dysplastic or Atypical Nevi) that present similar characteristics to melanomas [3]. It is consensual that the early diagnosis of malignant skin lesions (melanomas) is essential for the patient prognosis.

Recently, telemedicine techniques have been studied as a resource to obtain an early diagnosis of skin lesions. Besides the fact that dermatology probably is the most visual specialty in medicine, the teledermatology consultation brings some benefits, like easier access to health care and faster clinical results [4]. Comparing the physical examination (face-to-face diagnosis) with the remote diagnosis, experiments indicate that teledermatology is effective and reliable [5]. Teledermatology can benefit from image prescreening to help identify potentially malignant cases in their early stages.

To help distinguishing between benign and malignant cases, dermatologists often analyze each lesion with a dermoscope, which is a noninvasive tool that facilitates the evaluation of submacroscopic morphologic and vascular structures. As can be seen in Fig. 1, dermoscopy enables the generation of images with constant illumination, different texture patterns, and characteristics that are not measurable in standard camera images, such as lesion area and perimeter. In this way, many research groups developed digital dermoscopy image analysis schemes to help in skin lesion diagnosis [6].

In an attempt to prescreen/classify dermoscopy images, Celebi et al. [8] achieved 92.34% and 93.33% of specificity and sensitivity, respectively, using a JSEG-based segmentation algorithm and Support Vector Machines in the classification. More recently, Iyatomi et al. [9] proposed, to the best of our knowledge, the first publicly accessible system (“Dermatologist-like”), based on a region growing segmentation method and an Artificial Neural Network classifier. The user can upload an image at their website ‘<http://dermoscopy.k.hosei.ac.jp>’ and obtain a prescreening result. This system achieved a sensitivity of 85.9% and a specificity of 86.0% for a set of 1258 dermoscopy images [9].

Despite the importance of these efforts, a disadvantage of these methods is that they require dermoscopy images, and dermoscopes are not common among non-specialists. Moreover, studies indicate that dermoscopy images do not increase diagnosis accuracy in early stages [10]. So, with the proposal to facilitate the access to health care, also have been developed teledermatology systems making use of images acquired with standard cameras. In this way, patients do not need to go physically to a hospital or a clinic for a preliminary evaluation (even in benign cases), specially in remote areas. However, due to the already mentioned different visible character-

* Corresponding author. Tel.: +55 51 3308 7128; fax: +55 51 3308 7308.

E-mail addresses: pgcavalcanti@inf.ufrgs.br (P.G. Cavalcanti), jacobs@inf.ufrgs.br (J. Scharcanski).

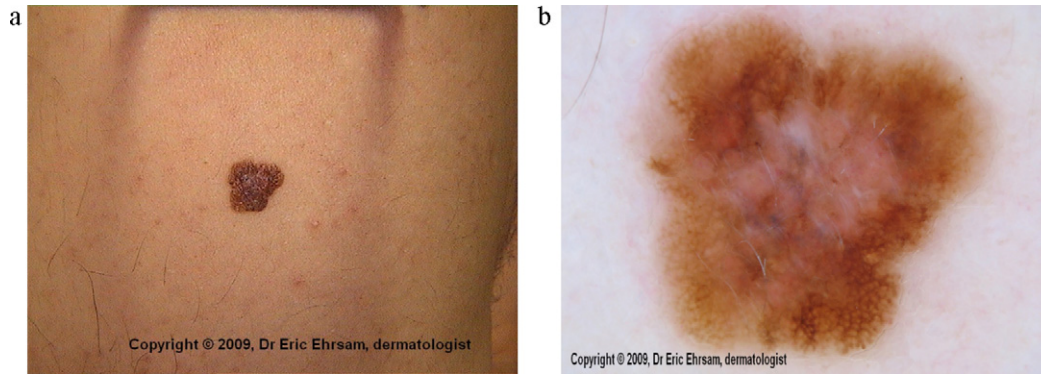


Fig. 1. Different visualizations of the same lesion using: (a) macroscopic image acquired with a standard camera; and (b) microscopic image acquired with a dermoscope (Courtesy of Eric Ehrsam, MD [7]).

istics in standard camera images and in dermoscopy images (see Fig. 1), these systems require different segmentation methods and feature extraction techniques.

A recent approach proposed by Alcon et al. [11] is an easy-to-use melanoma prescreening system based on standard camera images. A skin lesion photograph is provided as an input, and its prescreening is automatically produced, using segmentation and classification algorithms. However, often the acquired images contain artifacts, such as uneven illumination, which causes difficulties in the lesion segmentation stage, therefore their system initially corrects the image background. Afterwards, 55 features are extracted and the ABCD rule (Asymmetry, Border irregularity, Color variation and Differential structures) is employed to classify the lesion image as benign or malignant. Their system reaches an accuracy of 86.64% in its best performance [11].

This paper describes a new melanoma prescreening method using standard camera images and new techniques to improve the processing and analysis of such images, which was designed to be used remotely by non-specialists. In our experiments (see Section 6), we used 220 images obtained from two websites, with no special care in image acquisition or postprocessing. Each one of these images was submitted to a sequence of processing steps, namely: (1) preprocessing, where shading effects are attenuated by a new preprocessing stage proposed in this paper, as described in Section 2; (2) segmentation, where a new 3-channel image representation is proposed and used to discriminate between lesion and healthy skin areas, as described in Section 3; (3) feature extraction, where a quantitative lesion description containing new features extracted from our 3-channel representation is generated, as described in Section 4; and finally (4) lesion classification provides a lesion pre-diagnosis (using a hybrid classifier proposed in this paper); this processing step was designed to reduce the number of false negatives in the classification of skin lesion images as malignant or non-malignant, as described in Section 5. In Section 6, experimental results are presented, and Section 7 we present our conclusions.

2. Preprocessing

As mentioned before, the input image may be affected by illumination artifacts, and if used directly in the segmentation process, shading and lesion regions could be confused. Therefore, shading is attenuated in the input image before the image segmentation.

We start by converting the input image \tilde{I}_i^c ($\tilde{I}_i^c(x, y) \in [0, 1]$, $i = 1, 2, 3$) from the original RGB color space to the HSV color space \tilde{I}_i^{HSV} [12]. This is justified by the better shading visibility in the Value channel, and also by the simplicity of dealing with monochromatic images.

Let \tilde{I} be the Value normalized channel of \tilde{I}_i^{HSV} such that $\tilde{I} \in [0, 1]$. To correct the illumination in monochromatic images, Soille [13] suggests a simple operation:

$$R(x, y) = \frac{\tilde{I}(x, y)}{M(x, y)}, \quad (1)$$

where, R is the resultant image, $M = \tilde{I} \cdot s$ is the morphological closing of \tilde{I} by the structuring element s , and (x, y) represents a pixel in each one of these images. The main idea is that the closing operator is used to estimate the local illumination. However, Fig. 2(b) and (c) shows that the result is unsatisfactory, specially because it is difficult to determine an efficient structuring element for each image location, and the illumination is inhomogeneous.

Skin lesions often occur on curved surfaces (e.g. arms, hands, faces, etc.), and the illumination changes locally due to the surface curvature, generating shading effects. A smoothly darkening surface is presented as one that is turning away from the view direction, and we use shape from shading concepts [14,15] to relight the image (instead of determining the illumination variation by a morphological closing operation).

In order to avoid confusing lesion darkness with image shading, we capture shading information based on pixels known to be in healthy skin areas. The lesion is supposed to be in the central part of the image, which contains the lesion entirely, and healthy skin areas are expected in the four image corners [15–17]. Therefore, we use a set of 400 pixels around each image corner (20×20 square), and find the pixel set S as the union of the four pixel sets, corresponding to 1600 pixels associated to healthy skin. The pixel set S is used to determine the local illumination intensity $z(x, y)$, adjusting the following quadric function:

$$z(x, y) = P_1x^2 + P_2y^2 + P_3xy + P_4x + P_5y + P_6, \quad (2)$$

where, the six quadric function parameters P_i ($i = 1, \dots, 6$) are chosen to minimize the error ϵ :

$$\epsilon = \sum_{j=1}^{\#S} [\tilde{I}(S_{j,x}, S_{j,y}) - z(S_{j,x}, S_{j,y})]^2, \quad (3)$$

where, $S_{j,x}$ and $S_{j,y}$ are the x and y coordinates of the j th element of the set S , respectively.

Calculating the quadric function $z(x, y)$ for each image spatial location (x, y) , we estimate the local illumination intensity in the image \tilde{I} . Next, we replace $M(x, y)$ by $z(x, y)$ in Eq. (1) obtaining $R(x, y)$, significantly attenuating the shading effects (see Eq. (1)). An illustration of the results obtained with this shading attenuation approach is in Fig. 2(d) and (e). Next, the monochromatic image $R(x, y)$ is used to replace the Value channel \tilde{I}_3^{HSV} in \tilde{I}_i^{HSV} , and we obtain the shading corrected image by converting \tilde{I}_i^{HSV} to the orig-

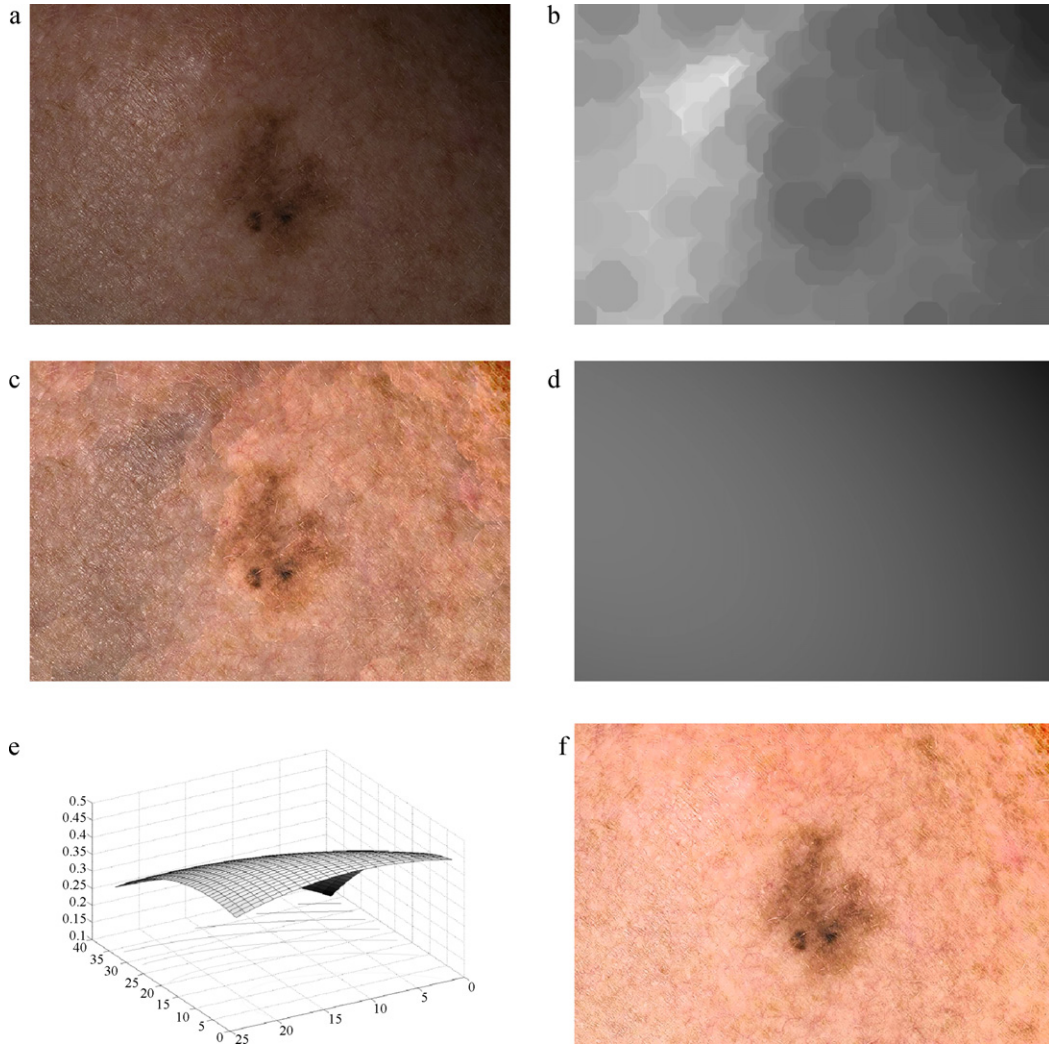


Fig. 2. Shading attenuation. (a) Input image; (b) closing of the input value channel by a disk of 30 pixels radius; (c) result obtained by replacing the input value channel by its normalized version using the image (b) – an unsatisfactory shading attenuation result; (d) obtained quadric model using the corners of the input value channel; (e) obtained quadric model in 3D; (f) result obtained by substituting the normalized version of the input value channel using the quadric model in (d) as a normalization factor – our shading attenuation result.

inal RGB color space \tilde{I}_i^c , $i = 1, 2, 3$. Examples of color images with shading correction are presented in Figs. 2(f) and 4(b).

3. Skin lesion segmentation

The skin lesion segmentation helps identify the skin lesion area and its rim in monochromatic [11,18], or in color [8,9] images. However, skin artifacts such as hair and freckles can be confused with lesions, and affect negatively the prescreening process (e.g., feature extraction and classification). Moreover, segmentation techniques developed for dermoscopy images consider texture and color patterns that are usually not visible in standard camera images. Thus, we propose a new method to segment the lesions in these kind of image.

To minimize segmentation errors, we create a new representation \tilde{I}_i^N ($i = 1, 2, 3$) from the original image to improve the discrimination between healthy and unhealthy skin regions. This new three-channel image contains normalized values ($\tilde{I}_i^N(x, y) \in [0, 1]$, $\tilde{I}_i^N(x, y) \in \mathbb{R}$), improving its sensitivity to local changes in the lesion characteristics (such as texture, darkness and color variation). The features represented more explicitly in each one of these three channels are discussed in Sections 3.1, 3.2 and 3.3.

3.1. Texture variability information channel (\tilde{I}_1^N)

Skin lesions often have more local textural variability than healthy skin areas, and that can be used to differentiate healthy and unhealthy skin regions. In order to capture the textural variation information we start by computing the normalized Luminance image \tilde{L} , defined as:

$$\tilde{L}(x, y) = \frac{\sum_{i=1}^3 \tilde{I}_i^c(x, y)}{3}, \quad (4)$$

where, $\tilde{I}_i^c(x, y)$ is a pixel (x, y) of the normalized RGB color image. We quantify the textural variability in $\tilde{L}(x, y)$ by computing $\tau(x, y, \sigma)$:

$$\tau(x, y, \sigma) = \frac{\tilde{L}(x, y)}{S(x, y, \sigma)} - \tilde{L}(x, y), \quad (5)$$

where, $S(x, y, \sigma) = \bar{L}(x, y) \times G(\sigma)$ (i.e., the Luminance image \bar{L} is smoothed by a Gaussian filter with standard deviation σ). Rearranging terms in Eq. (5), we obtain:

$$\begin{aligned}\tau(x, y, \sigma) &= \frac{\bar{L}(x, y) - \bar{L}(x, y) \cdot S(x, y, \sigma)}{S(x, y, \sigma)} \\ &= \frac{\bar{L}(x, y)(1 - S(x, y, \sigma))}{S(x, y, \sigma)} \\ &= \bar{L}(x, y) \frac{\tilde{S}(x, y, \sigma)}{S(x, y, \sigma)},\end{aligned}\quad (6)$$

where $\tilde{S}(x, y, \sigma)$ represents the complement of the \bar{L} smoothed image (i.e. $\tilde{S}(x, y, \sigma) = 1 - S(x, y, \sigma)$). If an image region is dark (i.e. has low pixel intensities, as often occurs in skin lesions), $\tilde{S}(x, y, \sigma) > S(x, y, \sigma)$ and the ratio $\tilde{S}(x, y, \sigma)/S(x, y, \sigma)$ tends to increase, and the local region and textural information are emphasized; if the region is bright (e.g. as in healthy skin regions), $\tilde{S}(x, y, \sigma) < S(x, y, \sigma)$ and the ratio $\tilde{S}(x, y, \sigma)/S(x, y, \sigma)$ tends to decrease, and the local region and its textural information are de-emphasized. This process is illustrated in Fig. 3 for the image shown in Fig. 2(f). Usually, most pixels in \bar{L} correspond to healthy skin (i.e., have higher intensity values). However, most skin pixels have lower values (closer to zero) in $\tau(x, y, \sigma)$, while skin lesion pixels tend to be brighter, as the histogram peaks show in Fig. 3(b) and (c).¹

A single Gaussian filter may not be sufficient to capture the textural variability of different types of lesions in generic images. So, we calculate $\tau(x, y, \sigma)$ for different σ values² $\{\sigma_1, \sigma_2, \dots, \sigma_N\}$, and select at each pixel the maximum $\tau(x, y, \sigma)$ among all scales σ :

$$T(x, y) = \max_{\sigma} [\tau(x, y, \sigma)], \quad \sigma \in \{\sigma_1, \sigma_2, \dots, \sigma_N\}. \quad (7)$$

Finally, the texture variation channel T is normalized, obtaining \bar{I}_1^N :

$$\bar{I}_1^N(x, y) = \frac{(T(x, y) - \min(T))}{(\max(T) - \min(T))}. \quad (8)$$

The procedure described in Eq. (7) was designed to capture the local texture variability information at each pixel (x, y) , in lesions of different sizes, shapes and texture patterns.

3.2. Local skin darkness information channel (\bar{I}_2^N)

We use the complement of $\bar{I}_2^N = 1 - \bar{I}_1^N(x, y)$ (i.e. the normalized Red channel) to represent the local skin darkness. Healthy skin tends to be reddish, so brighter $\bar{I}_1^N(x, y)$ pixels occur in healthy skin regions and darker $\bar{I}_1^N(x, y)$ pixels often occur in lesion areas. Therefore, \bar{I}_2^N tends to present lower intensity values in healthy skin areas and higher intensity values in lesion areas. Local skin darkness information \bar{I}_2^N is used to reinforce the local texture variability information in \bar{I}_1^N , and to help discriminate between healthy and unhealthy skin areas in the input image.

3.3. Color information channel (\bar{I}_3^N)

Usually, healthy and unhealthy skin present different color distributions. To reduce the problem dimensionality and represent the color information in a single channel, we use principal component analysis (PCA) [18,19].

Let \bar{c} be the color of the normalized RGB image pixel (x, y) , where $\bar{c} = [\bar{I}_1^N(x, y) \ \bar{I}_2^N(x, y) \ \bar{I}_3^N(x, y)]$. The PCA finds vectors $\bar{u}_1, \bar{u}_2, \bar{u}_3$ (arranged as columns of a matrix U) in such a way that $\bar{c}^T = U^T \bar{c}$

maximizes the spread (variance) of the RGB data. We want a single channel representation for the color variability information, and then only use the vector \bar{u}_1 pointing along the direction that maximizes the variance of \bar{c}_1^T (i.e. first component of \bar{c}^T). Assuming centered RGB data $\sum \bar{c}_i = 0$ (the color data is centered by subtracting the mean data vector $\bar{\mu}$, i.e. $\bar{c} = \bar{c} - \bar{\mu}$), \bar{u}_1 is the vector that maximizes $\sum_{i=1}^3 (\bar{u}_1^T \bar{c}_i)^2$. In other words, the image colors (3D points) projected along the \bar{u}_1 direction (1D scalars) are as spread as possible.

To make sure that lesion pixels have higher values than healthy skin pixels, as in the channels \bar{I}_1^N and \bar{I}_2^N , we use the PCA property described next. Since the color data is centered around the mean vector $\bar{\mu}$, and the most frequent colors are predominant in the computation of $\bar{\mu}$, the most frequent colors are projected along the \bar{u}_1 direction closer to the origin of the space spanned by \bar{c}_i . Since the healthy skin pixels usually are more frequent, their corresponding projection magnitudes $|\bar{c}_1^T| \approx 0$, however the lesion pixels projection magnitudes $|\bar{c}_1^T|$ tend to be larger than zero. Therefore, we represent the color variability information C by the magnitudes of \bar{c}_1^T (i.e., $C = |\bar{c}_1^T|$).

In the sequence, we normalize the C values at each pixel (x, y) and create the \bar{I}_3^N channel:

$$\bar{I}_3^N(x, y) = \frac{(C(x, y) - \min(C))}{(\max(C) - \min(C))}. \quad (9)$$

Also, we reduce the noise in \bar{I}_3^N by filtering it with a 5×5 median filter. The color information channel \bar{I}_3^N helps to discriminate between healthy and unhealthy skin pixels, while emphasizing skin lesion regions.

3.4. Skin lesion area segmentation and rim detection

In all three channels of the input image representation $\bar{I}_i^N(x, y)$, lesion pixels tend to have higher intensities than healthy skin pixels. Fig. 4 illustrates these images, and show that their histograms typically are bimodal (lesion/healthy skin). Therefore, we segment the lesion areas using a method inspired on the Otsu's thresholding method [20]. This algorithm assumes two pixel classes, usually healthy and unhealthy skin pixels, and searches exhaustively for the threshold th that minimizes the total intra-class variance $\sigma_w^2(th)$, defined as the weighted sum of variances of the two classes:

$$\sigma_w^2(th) = \omega_1(th)\sigma_1^2(th) + \omega_2(th)\sigma_2^2(th), \quad (10)$$

where ω_i are the a priori probabilities of the two classes separated by the threshold th , and σ_i^2 are their intra-class variances. Minimize the intra-class variance is equivalent to maximize the inter-class variance $\sigma_b^2(th)$:

$$\begin{aligned}\sigma_b^2(th) &= \sigma^2 - \sigma_w^2(th) \\ &= \omega_1(th)\omega_2(th)[\mu_1(th) - \mu_2(th)]^2,\end{aligned}\quad (11)$$

where σ^2 is the image pixels variance, and μ_i are the class means. Therefore, we obtain three thresholds th_i by maximizing $\sigma_b^2(th)$ for each \bar{I}_i^N channel, creating a lesion segmentation mask ϕ . A pixel (x, y) is in a lesion region (i.e., $\phi(x, y) = 1$) if its value is higher than the threshold th_i in at least two of the three channels:

$$\phi(x, y) = \begin{cases} 1, & \text{if } (\bar{I}_1^N(x, y) > th_1 \wedge \bar{I}_2^N(x, y) > th_2), \\ 1, & \text{if } (\bar{I}_2^N(x, y) > th_2 \wedge \bar{I}_3^N(x, y) > th_3), \\ 1, & \text{if } (\bar{I}_1^N(x, y) > th_1 \wedge \bar{I}_3^N(x, y) > th_3), \\ 0, & \text{otherwise.} \end{cases} \quad (12)$$

Although Ganster et al. [21] stated that a OR-combination of binary masks gives the best segmentation results, we noted in our

¹ The higher histogram peaks are associated to healthy skin regions in Fig. 3(b) and (c).

² In our experiments, we used $\sigma = 1, 11/7, 15/7, \dots, 43/7$, and filter window sizes of $7\sigma \times 7\sigma$.

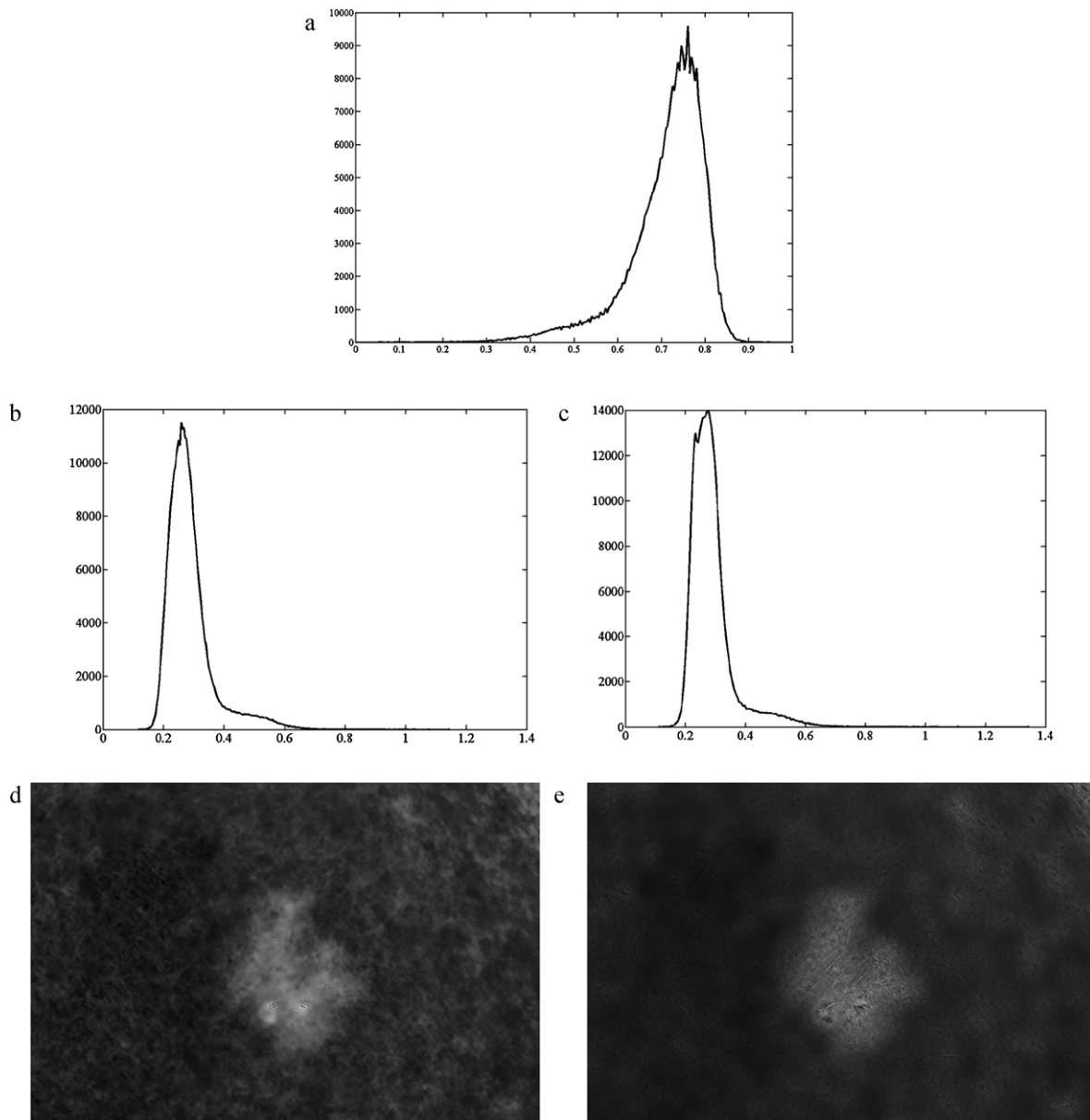


Fig. 3. Texture variability quantification $\tau(x, y, \sigma)$. (a) Histogram of the Luminance image \tilde{L} of Fig. 2(f); (b) and (c) show the histograms of $\tilde{L}(x, y)\tilde{S}(x, y, \sigma)/S(x, y, \sigma)$ (see Eq. (6)) using $\sigma = 1$ and $\sigma = 43/7$, respectively; (d) and (e) show the image instances associated to the histograms shown in (b) and (c).

experiments that this approach tends to merge lesion and healthy skin areas (e.g., areas where the skin have color or texture similar to lesions). In our approach, majority voting is used to eliminate most of these incorrectly segmented areas. After this operation, the remaining skin artifacts (such as freckles and hair) are eliminated more easily. These artifacts usually are form isolated regions that differ in area and perimeter from skin lesions, since lesions often have larger areas and boundaries that are more irregular. Therefore, we compute the perimeter and the area of all thresholded connected pixel sets (i.e. where $\phi(x, y) = 1$), and then partition this set of regions in two clusters. All regions in the cluster with smaller areas (in average) are eliminated, and we set their mask pixels to $\phi(x, y) = 0$.

After eliminating artifacts, the lesion regions still can contain rim imperfections (caused by hair or noise), which we filter out by applying a 5×5 median filter to $\phi(x, y)$. Fig. 5(a)–(c) illustrates the lesion area segmentation steps (i.e., thresholding, artifacts elimination and filtering) for the image shown in Fig. 4(b). As it can

be seen, there can be holes inside the lesion segment, but their pixels are not considered further in the next image processing steps of our method. These holes often occur because of image specularities, and these pixels are not processed further because they could introduce noise in the lesion feature extraction process. The obtained lesion rim (i.e., the outer perimeter of the lesion) is shown in Fig. 5(d) superimposed to the original image (Fig. 4(b)).

4. Feature extraction

We extract a set of image features to distinguish between benign and malignant skin lesions. Given the segmentation results, we compute the local characteristics from the lesion areas according to the ABCD rule [22]. The ABCD acronym refers to the four criteria used in this rule, namely: Asymmetry, Border irregularity, Color variation and Differential structures.

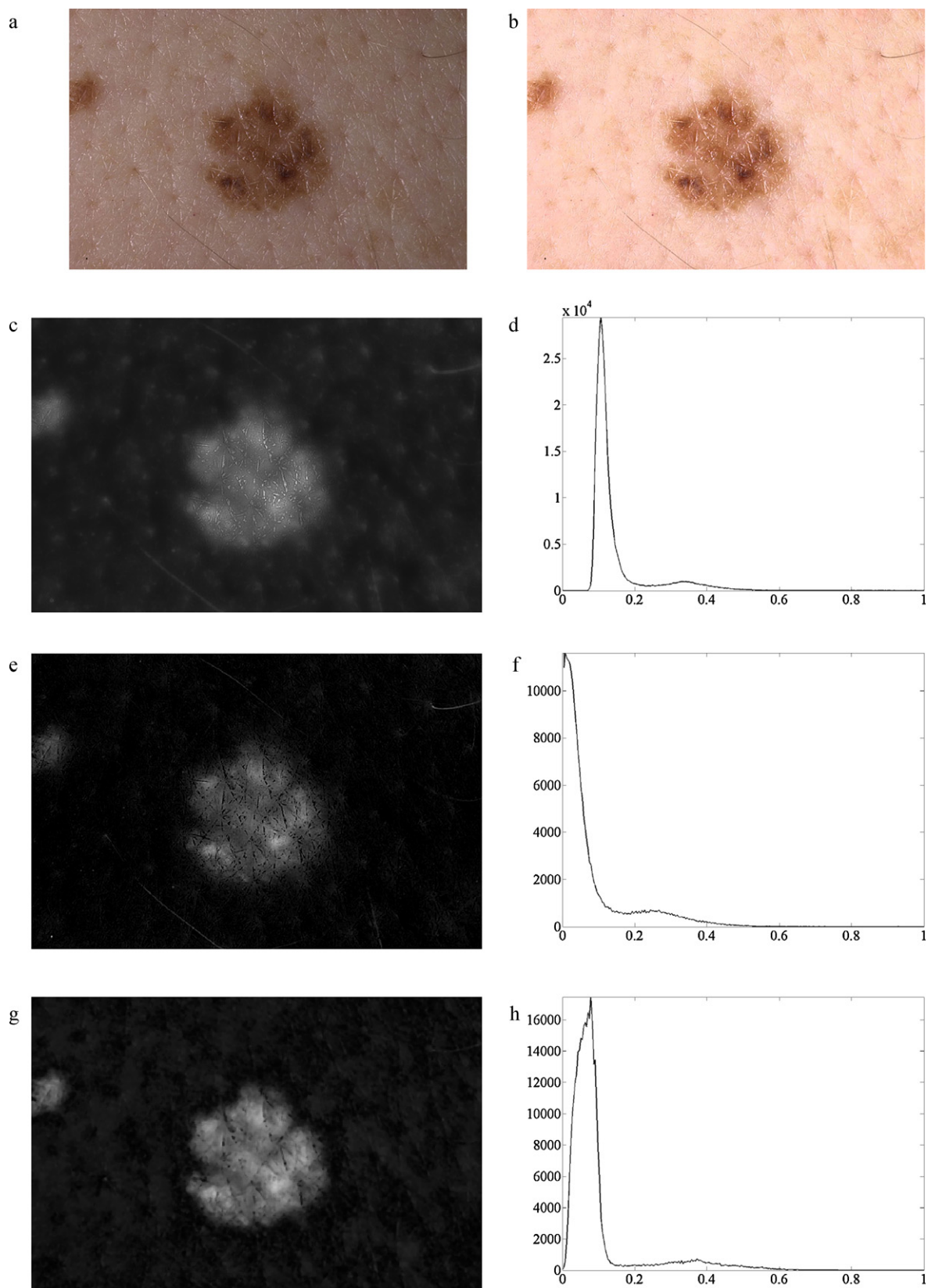


Fig. 4. Illustration of our 3-channel image representation \bar{T}_i^N and the data bimodal distribution in each channel (in higher peaks of histograms the healthy skin pixels, and in lower peaks the lesion pixels). (a) Input image; (b) input image after shading attenuation; (c) and (d) show the computed texture variability information channel (\bar{T}_1^N) and its histogram; (e) and (f) show the computed local skin darkness information channel (\bar{T}_2^N) and its histogram; (g) and (h) show the computed color information channel (\bar{T}_3^N) and its histogram.

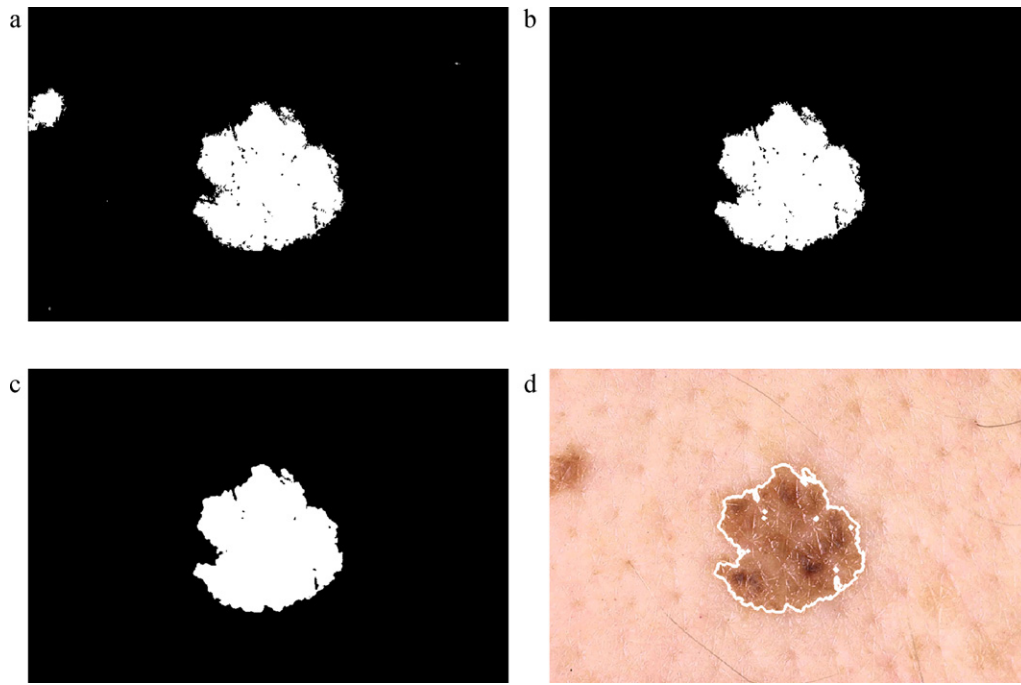


Fig. 5. Segmentation process for the image shown in Fig. 4(b). (a)–(c) show the lesion segmentation masks $\phi(x, y)$, respectively, after thresholding, artifacts elimination and filtering; (d) shows the computed lesion rim (dilated by two pixels for better visualization) superimposed to the original image.

The ABCD rule in important dermatology, and most dermatological prescreening systems rely on some scheme for quantifying the four criteria of the ABCD rule. In this work, we propose some image features to quantify this rule, and combine them with other features that have already been proposed in the literature.

4.1. Features used for lesion asymmetry characterization

The goal of the proposed features is to quantify the lesion shape, in special the asymmetry of the lesion in relation to the principal axes. The major axis L_1 of the lesion is aligned with its longest diameter, passing through its center; the minor axis L_2 is orthogonal to L_1 and also passes through the shape center. The selected features are:

- f_1 : Solidity: the ratio between the lesion area (A) and its convex hull area [11];
- f_2 : Extent: the ratio between the lesion area and its bounding box area [11];
- f_3 : Equivalent diameter: $4A/(L_1\pi)$ [11,8];
- f_4 : Circularity: $4\pi A/(L_1p)$, where p is the lesion perimeter [11];
- f_5 : The ratio between the principal axes (L_2/L_1) [11,8];
- f_6 : The ratio between sides of the lesion bounding box [11];
- f_7 : The ratio between the lesion perimeter p and its area A [23];
- f_8 : $(B_1 - B_2)/A$, where, B_1 and B_2 are the areas in each side of axis L_1 ;
- f_9 : Similar to f_8 , but makes use of the shorter axis L_2 ;
- f_{10} : B_1/B_2 with respect to the axis L_1 ;
- f_{11} : Similar to f_{10} , but makes use of the shorter axis L_2 .

4.2. Features used for lesion boundary irregularity characterization

The boundary sharpness is quantified by the magnitude of the gradient $\left| \nabla \vec{I}_i^N \right|$ at each pixel using the Sobel operator. However,

instead of using pixels only at the lesion rim, we analyze pixels in an extended (dilated) rim³[11]. Consequently, lesions that have a smooth boundary (usually nevi) are better characterized. Also, the lesion boundary dilation makes the boundary representation more robust to the inaccuracies of the segmentation process. To characterize the lesion boundary irregularity, we use the following features:

- f_{12} – f_{14} : Average gradient magnitude of the pixels in the lesion extended rim [11], in each one of the three I_i^N channels;
- f_{15} – f_{17} : Variance of the gradient magnitude of the pixels in the lesion extended rim [11], in each one of the three I_i^N channels;

The lesion rim irregularity is characterized in the ABCD rule by dividing the rim in 8 symmetric regions [22]. In addition to the two principal axes L_1 and L_2 , we rotate these orthogonal axes by 45 degrees and obtain two additional axes. Therefore, 8 symmetric regions $R = 1, \dots, 8$ are obtained. For each channel I_i^N , the average gradient magnitudes of the extended rim pixels $\mu_{R,i}(R = 1, \dots, 8)$ are computed. Therefore, we calculate 6 more features:

- f_{18} – f_{20} : Average of the 8 $\mu_{R,i}$ values in each one of the three I_i^N channels;
- f_{21} – f_{23} : Variance of the 8 $\mu_{R,i}$ values in each one of the three I_i^N channels.

4.3. Features used for lesion color variation characterization

Their goal is to quantify the color variation in the lesion. The selected features are:

- f_{24} – f_{27} : Maximum, minimum, mean and variance of the pixels intensities inside the lesion segment in the color variation channel I_i^N ;

³ The rim is dilated by 2 pixels, producing a 5 pixels wide region centered at the lesion rim, as suggested in [11].

Table 1
Six possible colors of a lesion on the RGB color space.

Color	Red	Green	Blue
White	1	1	1
Red	0.8	0.2	0.2
Light brown	0.6	0.4	0
Dark brown	0.2	0	0
Blue-gray	0.2	0.6	0.6
Black	0	0	0

- f_{28} – f_{39} : Maximum (f_{28} – f_{30}), minimum (f_{31} – f_{33}), mean (f_{34} – f_{36}) and variance (f_{37} – f_{39}) of the intensities of pixels inside the lesion segment, in each one of three original \tilde{I}_i^c channels;
- f_{40} – f_{42} : Ratios between mean values of the tree original \tilde{I}_i^c channels: $mean(\tilde{I}_1^c)/mean(\tilde{I}_2^c)$, $mean(\tilde{I}_1^c)/mean(\tilde{I}_3^c)$ and $mean(\tilde{I}_2^c)/mean(\tilde{I}_3^c)$, considering only pixels inside the lesion segment.

Physicians usually identify six distinct hues in skin lesions: white, red, light and dark brown, blue-gray, and black [22]. Lesions containing more of these hues are more likely to be malignant. We quantify the lesion color variability by computing the occurrence of these typical hues within a lesion segment. Given a pixel in the lesion segment, we find the nearest reference color (associated with a typical hue, see Table 1 [11]) by the Euclidean distance to the pixel color in \tilde{I}_i^c . A hue occurrence counter is created, one cell per typical hue. For each lesion pixel, the nearest typical hue counter is increased by 1. Finally, typical hues counters are normalized/divided by the lesion area A , and generate the 6 additional features f_{43} – f_{48} .

4.4. Features used for lesion differential structures characterization

The lesion differential structures refer to submacroscopic morphologic and vascular structures only visible in dermoscope images, as already mentioned in Section 1. However, we measure differences between benign and malignant lesions using texture features found in macroscopic images. We extract the 4 features f_{49} – f_{52} , namely the maximum, minimum, mean and variance of the pixels intensities inside the lesion segment to represent the textural variation in the channel \tilde{I}_1^N .

5. Lesion classification

After segmenting a lesion segment, and extracting 52 features f_1 – f_{52} (see Section 4), we can discriminate a benign from a malignant pigmented skin lesion by classification. We present in the following subsections our classification scheme.

5.1. Feature normalization

The extracted features may generate values in different ranges. However, often classifiers are more efficient if these feature values are normalized (produce values within a specified range). We normalize feature values with the z-score transformation [24]:

$$Z_{i,j} = \frac{((v_{i,j} - \mu_j)/(3\sigma_j) + 1)}{2}, \quad (13)$$

where, $v_{i,j}$ is the value of the j th feature of the i th sample (image), μ_j and σ_j are the mean and standard deviation of the j th feature, respectively. After the z-score transformation, most of the $Z_{i,j}$ values are in the $[0,1]$ range. The out-of-range values are saturated to either 0 or 1.

5.2. Training samples selection

We applied holdout validation for the training samples selection. That is, half of the samples in each class (benign or malignant) are randomly selected for the training set. Additionally, since we have a relatively small image data set (with N samples described in Section 6), new samples are added to the training set using the Smoothed Bootstrap Resampling method⁴ to obtain η samples, where $\eta > N$. In our experiments, we used zero mean Gaussian noise with $\sigma = 0.1$, obtained $\eta/2$ samples for each class, and η was set to the interval $[1000, 5000]$ (see Section 6).

5.3. Classification

Two classifiers are used in our experiments (see Section 6), namely the K -nearest neighbors (KNN) classifier, and the KNN followed by a Decision Tree classifier (KNN-DT). Detailed information about these classifiers are presented next.

- KNN: classifies samples based on K closest matches in feature space [26]. We use $K=1$ and each sample is assigned to its nearest neighbor class by using the Euclidean distance. Although this classifier have already been used in previous approaches [27,28], it never resulted in a high accuracy as with our proposed features (see our experiments in Section 6).
- KNN-DT: uses the KNN classifier (above) and a set of Bayes' Classifiers, each specialized on a feature sub-set identified by the Classification and Regression Tree (CART) method [29]. It is used to reduce false negatives by confirming each case pre-diagnosed as benign by KNN.

The Bayes' Classifier [26] assigns a sample to the most likely class, given the extracted features. Let L be a set of features $[f_1, \dots, f_{52}]$ extracted from a lesion, $D=1$ the malignant class and $D=0$ the benign class. Using Bayes' rule, the posterior probability $P(D|L)$ of assigning a lesion to class D can be written as:

$$P(D|L) = \frac{P(L|D)P(D)}{P(L)}, \quad (14)$$

where, $P(L|D)$ is the conditional probability of finding a lesion with these L characteristics in class D , $P(D)$ is the prior probability of class D , and $P(L)$ is the evidence and it represents the probability that these features L are seen.

Since the evidence $P(L)$ will be the same for both classes ($D=0$ and $D=1$), we discard this term from Eq. (14), and the lesion can be considered malignant if $P(D=1|L) > P(D=0|L)$, or if:

$$P(L|D=1)P(D=1) > P(L|D=0)P(D=0), \quad (15)$$

and it is benign otherwise. Given adequate estimates of $P(L|D)$ and $P(D)$, the Bayes' Classifier is optimal since it minimizes the probability classification error. Considering that we have a relatively large feature set to discriminate reliably between nevi and melanomas (see the proposed 52 features in Section 4), the estimate of the joint feature probability in Eq. (15) can be quite challenging without simplifications. Also, $P(D)$ is not known (to the best of our knowledge). Therefore, we use CART to simplify these estimates. Recall that we are interested in minimizing false malignant (melanoma) negatives by confirming the pre-diagnosis of nevi cases. Therefore, we simplify our problem by choosing feature sub-sets (with less than 52 features) that independently can provide evidences for a melanoma

⁴ The Smoothed Bootstrap Resampling method is used when data is not sufficient to guarantee statistical significance. Specifically, original samples are randomly selected, and new ones are created adding a small amount of zero-centered noise to their feature values, enlarging the data set [25].

Table 2

The seven features most frequently encountered in all feature sub-sets generated by the KNN-DT classifier.

Feature	Percentage of sub-sets including the feature
f_{30}	100
f_1	88.61
f_{16}	88.61
f_{50}	56.91
f_4	54.47
f_{44}	52.84
f_8	51.21

pre-diagnosis, and the CART method is used to find these feature sub-sets.

The CART algorithm [29] iteratively builds a decision tree by creating feature space binary partitions (i.e. selecting linear feature discriminants), in a way that sample class homogeneity is increased within each sub-space partition at each decision tree construction step [26]. Each step introduces a new tree node (i.e. a new linear discriminant), and the CART algorithm converges when the sample class partitions are maximally homogeneous, given an error criterion. Traversing the decision tree from its root to a given leaf node, implies in testing a set of feature thresholds to reach a decision at the leaf node (i.e. reaching a sub-space partition that allows to decide whether to assign a sample to the nevus or the melanoma class). However, in this work we are only interested in the CART feature sub-sets involved in the leaf nodes decisions (not in the linear discriminants produced by CART). Particularly, we are interested in the feature sub-sets found by the CART algorithm that are used to decide the assignment of a sample to the melanoma class (i.e. in the decision tree leaf nodes involved in class $D=1$ assignment decisions). In this way, we reduce the computation of joint feature probability estimates in Eq. (15) to a set of feature sub-sets joint probability estimates, specially those used in $D=1$ class assignments. In this way, we reduce the chance of occurring false negatives in the final classification results (i.e. malignant samples incorrectly assigned to the non-malignant class can be re-assigned correctly).

In our experiments, we used $\eta=5000$ (see more details in Section 6) and obtained feature sub-sets of 4–19 features. In Fig. 6 we present a histogram of the number of features in all obtained feature sub-set, showing that most feature sub-sets involve 12 features. Table 2 shows the features positioned in the top 3 levels of the classification tree generated by the CART algorithm, which consequently are the 7 most frequently encountered features in all the obtained feature sub-sets.

The following steps are used to estimate the joint probabilities in these feature sub-sets:

- Considering all training samples assigned to classes $D=1$ and $D=0$ at all the leaf nodes, we estimate the prior class probabilities $P(D=1)$ and $P(D=0)$ as the percentages of the training set samples that are assigned to each one of these two classes. In fact, we calculate the probability that a sample is assigned to the class $D=1$ at any decision tree leaf node $P(D=1)$, and then estimate the prior probability that a sample is assigned to class $D=0$ as $P(D=0)=1-P(D=1)$;
- Considering all training samples, we compute the feature joint probabilities $P(L_l|D=0)$ and $P(L_l|D=1)$ for each decision tree branch leading to a $D=1$ class assignment, where L_l denotes all the features involved in the decision sequence at a given tree branch, from the tree root to its leaf node l . The feature joint probabilities $P(L_l|D=0)$ and $P(L_l|D=1)$ are multivariate distributions, that we model using an unsupervised modified EM (Expectation-Maximization) algorithm to identify finite Gaussian

mixture models based on the method proposed by Figueiredo and Jain [30];

- We calculate $P(L_l|D=0)$ and $P(L_l|D=1)$ for each leaf node l . Given the estimated $P(D=1)$ and $P(D=0)$, we use Eq. (15) at each leaf node with a $D=1$ class assignment decision, and decide if the sample in question should be re-assigned to the class $D=1$. For all leaf nodes l involving a $D=1$ assignment decision, we increment the counter $C_{D=1}$ if $P(L_l|D=1)P(D=1) > P(L_l|D=0)P(D=0)$;
- Finally, a sample previously assigned to the nevus class ($D=0$) is re-assigned to the melanoma class ($D=1$) is $C_{D=1} \geq N_l/2$, i.e. when at least half of the leaf node tests ($D=1$) indicate that the sample should be assigned to class $D=1$.

6. Experimental results and discussion

We used in our experiments two datasets of images: (a) the dataset used by Alcon et al. [11], with 152 images from the Dermnet dataset [31] (i.e., 45 benign Clark Nevi and 107 Melanomas); and (b) an extended dataset, which was built by adding 68 extra images from the DermQuest dataset [32] (37 Clark Nevi and 31 Melanomas), constituting a total of 82 Clark Nevi and 138 Melanomas in this extended dataset. The idea is to test our method in a dataset used in the literature (i.e. the Alcon et al. dataset [11]), and then confirm our method performance in a larger dataset. Most of the 220 images are 720 pixels in width in landscape format, or have a height of 720 pixels in portrait format. All images with different dimensions were resized to have 720 pixels in width or in height, preserving the aspect ratio. Recall that the imaged lesion is supposed to be in the central part of the image, and healthy skin areas are expected in the four image corners [16,17].

We compare our results with two representative methods reported in the literature: (a) Iyatomi et al. (known as the “Dermatologist-like”) [9], which is a publicly accessible telermatology prescreening system; and (b) Alcon et al. [11], which is the most recent approach dealing with standard camera images. In order to compare our results with these methods results, we use sensitivity ($Sens = (TP)/(TP + FN)$), specificity ($Spec = (TN)/(TN + FP)$) and accuracy ($Acc = (TP + TN)/(TP + FP + TN + FN)$), where TP , TN , FP and FN are, respectively, the number of True Positive, True Negative, False Positive and False Negative cases. Specifically, $Sens$ indicates the percentage of malignant (melanomas) cases correctly classified; $Spec$ indicates the percentage of benign (nevi) cases correctly classified; and, Acc indicates the overall percentage of cases correctly classified.

In order to illustrate that dermoscopy image prescreening methods actually are not adequate to analyze skin lesion images acquired with standard cameras, we tested the Alcon et al. dataset [11] in the web-based “Dermatologist-like” system [9]. From 107 melanomas images, 68 images were classified correctly, 26 images were mistakenly classified as nevi, 11 images were classified as ‘suspicious’ and 2 images resulted in no classification at all (probably because of segmentation errors). From 45 nevi images, 31 images were classified correctly, 7 images were incorrectly classified as melanomas, 5 images were classified as ‘suspicious’, and 2 resulted in no classification at all. In this experiment, we obtained a sensitivity of 75.24%, a specificity of 80%, and an accuracy of 75.66%, considering ‘suspicious’ as a correct classification, and the situation of ‘no classification’ as an incorrect classification.

Alcon et al. [11] tested two classification procedures in their dataset. They tested the Correlation-Based Feature Selector (CFS) with Logistic Model Tree (LMT), and classified correctly 101 images in 107 melanoma images, and 31 images in 45 nevi images, achieving a sensitivity of 94.39%, a specificity of 68.89% and an accuracy of 86.84%. The second classifier, CFS with Adaboost and LMT, classified correctly 96 images in 107 melanoma images, and 34 images

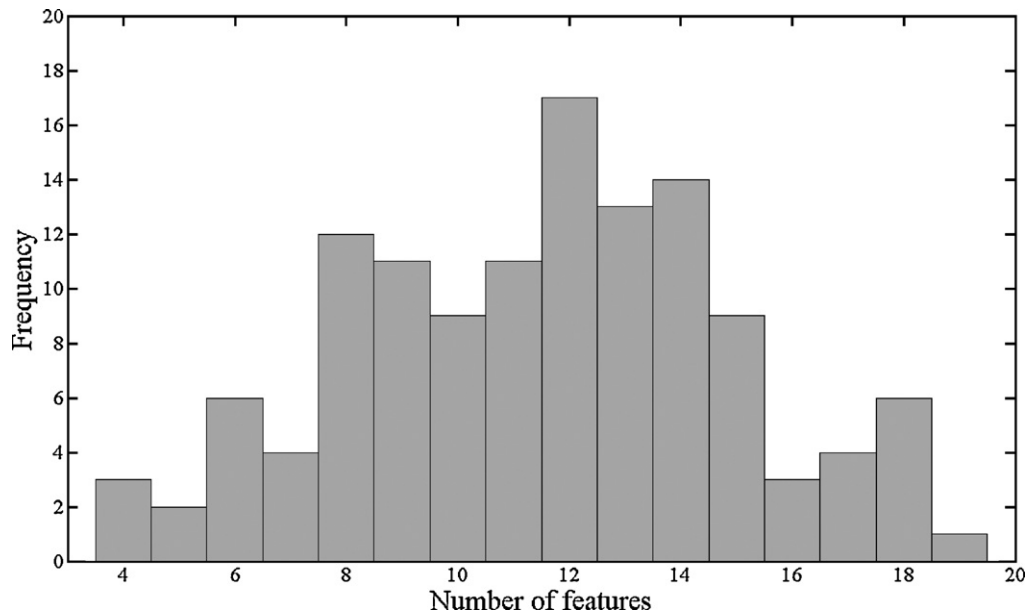


Fig. 6. Histogram of the number of features in all feature sub-sets generated by the KNN-DT classifier.

Table 3

Our experiments results using the Alcon et al. dataset.

Method	η	Melanomas class (total: 107)	Nevi class (total: 45)	Sens	Spec	Acc
KNN	1000	103	43	96.26%	95.55%	96.05%
KNN-DT	1000	103	43	96.26%	95.55%	96.05%
KNN	2000	102	43	95.32%	95.55%	95.39%
KNN-DT	2000	103	43	96.26%	95.55%	96.05%
KNN	3000	100	43	93.45%	95.55%	94.07%
KNN-DT	3000	102	43	95.32%	95.55%	95.39%
KNN	4000	101	43	94.39%	95.55%	94.73%
KNN-DT	4000	103	43	96.26%	95.55%	96.05%
KNN	5000	103	44	96.26%	97.77%	96.71%
KNN-DT	5000	103	44	96.26%	97.77%	96.71%

in 45 nevi images, achieving a sensitivity of 89.72%, a specificity of 75.56% and an accuracy of 85.53%.

Table 3 presents the results obtained with the Alcon et al. dataset, using our lesion image representation with the KNN and the KNN-DT classifiers, and different values of η (the number of Bootstrap samples). Although results are very similar, $\eta = 5000$ was selected since it maximize the accuracy (i.e., generated the highest number of correctly classified images). It is important to observe that the KNN-DT classifier tends to reduce the number of false negatives compared with the KNN classifier (i.e., correctly classified a higher number of melanoma/malignant images), obtaining higher sensitivity values.

Table 4 compares the results obtained by our approach ($\eta = 5000$), and by the methods proposed by Iyatomi et al. [9] and Alcon et al. [11], using the Alcon et al. dataset. As it can be seen that for the same dataset, the results obtained by our approach improved significantly on the results obtained by the other methods [9,11]. The highest accuracy result achieved by these methods

was 86.84% [11], and our approach achieved 96.71%, meaning that nearly 10% more cases of the dataset were classified correctly by our method. Also, our approach classified correctly more melanoma images, increasing the sensitivity values, and more nevi images, increasing significantly the specificity values.

As already mentioned, we also realized experiments with an extended image dataset. The KNN classifier classified correctly 131 images in 138 melanoma images, and classified correctly 75 images in 82 nevi images, achieving a sensitivity of 94.92%, a specificity of 91.46% and an accuracy of 93.63%. The KNN-DT classifier classified correctly 133 images in 138 melanoma images, and classified correctly the same 75 images in 82 nevi images (as the KNN classifier), achieving a sensitivity of 96.37%, a specificity of 91.46% and an accuracy of 94.54%. These results are shown in Table 5. Comparing with the results for the Alcon et al. dataset, we had a decrease in specificity. However, it is important to observe that our approach can correctly classify higher percentages of melanoma and nevi images, achieving better sensitivity, specificity and accuracy measures as compared to the other methods [9,11] (see Table 4).

Table 4

Comparison of results.

Method	Sens	Spec	Acc
"Dermatologist-like" [9]	75.24%	80%	75.66%
CFS with LMT [11]	94.39%	68.89%	86.84%
CFS with Adaboost and LMT [11]	89.72%	75.56%	85.53%
KNN	96.26%	97.78%	96.71%
KNN-DT	96.26%	97.78%	96.71%

Table 5

Results to the extended dataset.

Method	Melanomas class (total: 138)	Nevi class (total: 82)	Sens	Spec	Acc
KNN	131	75	94.92%	91.46%	93.63%
KNN-DT	133	75	96.37%	91.46%	94.54%

As can be seen in Tables 3 and 5, the KNN-DT classifier is able to classify correctly a higher number of melanoma images, and consequently it can provide higher sensitivity values than the KNN classifier. However, the KNN classifier can be useful since it has lower computational cost.

7. Conclusion

This paper presented a method for classifying pigmented skin lesions as benign or malignant. It is assumed that the lesion is located in the central part of the image, which contains the lesion entirely, and healthy skin areas are expected in the four image corners [16,17]. Besides the lesion position in the image, no special care is required in the skin lesion image acquisition (e.g. dermoscopy is not used), and the images are acquired with standard cameras and standard illumination, making our method suitable for telemedicine applications. Since our skin lesion pre-screening method is automatic, it can be used by non-specialists.

In this paper, new techniques to improve the processing and analysis of skin images acquired with standard cameras were proposed, such as: (1) a data-driven shading attenuation stage was introduced to preprocess the image and improve the robustness of the skin lesion segmentation; (2) to facilitate the lesion rim detection, a new 3-channel image representation that maximizes the discrimination between the lesion and healthy skin regions was presented; (3) to better discriminate between malignant and non-malignant lesions, new features based in our new 3-channel representation were introduced; and, (4) a hybrid classifier was proposed to reduce the number of false negatives in the classification of skin lesion images as malignant or non-malignant.

The preliminary experimental results suggest that our approach potentially can achieve better classification results than comparable methods available in the literature [9,11]. Using the dataset proposed in [11], the highest accuracy result achieved by these other methods was 86.84% [11], while our approach achieved 96.71% of accuracy. Also, our approach classified correctly more melanoma images, increasing the sensitivity values, and more nevi images, increasing the specificity values. Also, using an extended dataset, our method classified correctly 94.54% of the 220 images, with a sensitivity of 96.37% and a specificity of 91.46%. These experimental results are encouraging, and we plan to further develop our approach by improving the lesion segmentation and classification stages, and test more extensively our method in clinical trials.

References

- [1] Melanoma Research Project, Background; 2010. <http://www.melresproj.com/net/02.001.html>.
- [2] World Health Organization, How common is skin cancer?; 2010. <http://www.who.int/uv/faq/skincancer/en/index1.html>.
- [3] The Skin Site, Atypical moles; 2010. <http://www.skinsite.com/info.atypical.moles.htm>.
- [4] Massone C, Wurm EMT, Hofmann-Wellenhof R, Soyer HP. Teledermatology: an update. *Semin Cutan Med Surg* 2008;27:101–5.
- [5] Whited JD. Teledermatology research review. *Int J Dermatol* 2006;45:220–9.
- [6] Blum A, Zalaudek I, Argenziano G. Digital image analysis for diagnosis of skin tumors. *Semin Cutan Med Surg* 2008;27:11–5.
- [7] E. Ehrsam, Dermoscopy; 2010. <http://dermoscopic.blogspot.com/>.
- [8] Celebi ME, Kingravi HA, Uddin B, Iyatomi H, Aslandogan YA, Stoecker WV, et al. A methodological approach to the classification of dermoscopy images. *Comput Med Imaging Graph* 2007;31:362–73.
- [9] Iyatomi H, Oka H, Celebi M, Hashimoto M, Hagiwara M, Tanaka M, et al. An improved internet-based melanoma screening system with dermatologist-like tumor area extraction algorithm. *Comput Med Imaging Graph* 2008;32:566–79.
- [10] Skvara H, Teban L, Fiebigler M, Binder M, Kittler H. Limitations of dermoscopy in the recognition of melanoma. *Arch Dermatol* 2005;141:155–60.
- [11] Alcon JF, Ciuhu C, ten Kate W, Heinrich A, Uzunbajakava N, Krekels G, et al. Automatic imaging system with decision support for inspection of pigmented skin lesions and melanoma diagnosis. *IEEE J Select Top Signal Process* 2009;3:14–25.
- [12] Smith AR. Color gamut transform pairs. *SIGGRAPH Comput Graph* 1978;12:12–9.
- [13] Soille P. Morphological operators. In: Jähne B, Haussecker H, Geißler P, editors. *Handbook of computer vision and applications*, vol. 2. San Diego: Academic Press; 1999. p. 627–82.
- [14] Shapiro L, Stockman G. *Computer vision*. Prentice Hall; 2001.
- [15] Cavalcanti PG, Scharcanski J, Lopes CBO. Shading attenuation in human skin color images. In: *Proc., 6th., International Symposium on Visual Computing (ISVC, 2000)*, in press, doi:10.1007/978-3-642-17289-2.19.
- [16] Celebi ME, Kingravi HA, Iyatomi H, Aslandogan YA, Stoecker WV, Moss RH, et al. Border detection in dermoscopy images using statistical region merging. *Skin Res Technol* 2008;347–53.
- [17] Melli R, Grana C, Cucchiara R. Comparison of color clustering algorithms for segmentation of dermatological images. In: Reinhardt JM, Pluim JPW, editors. *Medical Imaging 2006: Image Processing*, vol. 6144, SPIE; 2006.
- [18] Gomez DD, Butakoff C, Ersboll BK, Stoecker W. Independent histogram pursuit for segmentation of skin lesions. *IEEE Trans Biomed Eng* 2008;55:157–61.
- [19] Celebi M, Iyatomi H, Schaefer G, Stoecker WV. Lesion border detection in dermoscopy images. *Comput Med Imaging Graph* 2009;33:148–53.
- [20] Otsu N. A threshold selection method from gray-level histograms. *IEEE Trans Syst, Man Cybern* 1979;9:62–6.
- [21] Ganster H, Pinz A, Rhner R, Wildling E, Binder M, Kittler H. Automated melanoma recognition. *IEEE Trans Med Imaging* 2001;20:233–9.
- [22] Nachbar F, Stolz W, Merkle T, Cognetta AB, Vogt T, Landthaler M, et al. The abcd rule of dermatoscopy: high prospective value in the diagnosis of doubtful melanocytic skin lesions. *J Am Acad Dermatol* 1994;30:551–9.
- [23] Fikrle T, Pizinger K. Digital computer analysis of dermatoscopic images of 260 melanocytic skin lesions; perimeter/area ratio for the differentiation between malignant melanomas and melanocytic nevi. *J Eur Acad Dermatol Venereol* 2007;21:48–55.
- [24] Haralick RM, Aksoy S, Haralick RM. Probabilistic vs. geometric similarity measures for image retrieval. In: *Proc. IEEE Conference on Computer Vision and Pattern Recognition*, vol. 2, p. 357–62.
- [25] Young GA. Alternative smoothed bootstraps. *J R Stat Soc Ser B (Methodological)* 1990;52:477–84.
- [26] Alpaydin E. *Introduction to machine learning (adaptive computation and machine learning)*. The MIT Press; 2004.
- [27] Dreiseitl S, Ohno-Machado L, Kittler H, Vinterbo S, Billhardt H, Binder M. A comparison of machine learning methods for the diagnosis of pigmented skin lesions. *J Biomed Inform* 2001;28–36.
- [28] Burroni M, Corona R, Dell'Eva G, Sera F, Bono R, Puddu P, et al. Melanoma computer-aided diagnosis: reliability and feasibility study. *Clin Cancer Res* 2004;10:1881–6.
- [29] Breiman L, Friedman JH, Olshen RA, Stone CJ. *Classification and regression trees*. New York, NY: Chapman & Hall; 1984.
- [30] Figueiredo MAF, Jain AK. Unsupervised learning of finite mixture models. *IEEE Trans Pattern Anal Mach Intell* 2002;24:381–96.
- [31] Dermnet, Skin disease image atlas; 2010. <http://www.dermnet.com>.
- [32] DermQuest.com, The art, science and practice of dermatology; 2010. <http://www.dermquest.com/>.